Optics Letters

Experimental realization of a reconfigurable Lieb photonic lattice in a coherent atomic medium

Shun Liang, Zhenzhi Liu, Shaohuan Ning, Yanpeng Zhang, and Zhaoyang Zhang*

Key Laboratory for Physical Electronics and Devices of the Ministry of Education & Shaanxi Key Lab of Information Photonic Technique, School of Electronic Science and Engineering, Faculty of Electronic and Information Engineering, Xi'an Jiaotong University, Xi'an 710049, China
**Corresponding author: zhyzhang@xjtu.edu.cn*

Received 5 September 2022; revised 26 December 2022; accepted 4 January 2023; posted 4 January 2023; published 31 January 2023

We have experimentally demonstrated the realization of an instantaneously reconfigurable Lieb photonic lattice with a flatband in a three-level Λ-type rubidium atomic configuration. Such a coherently controllable Lieb photonic lattice is optically induced by a coupling field possessing a spatially periodic intensity distribution (generated via a spatial light modulator) under the condition of electromagnetically induced transparency. The incident weak Gaussian probe field can experience discrete diffraction and the observed probe beam at the output surface of the medium exhibits the same Lieb pattern, verifying the formation of the refractive index with a Lieb profile inside the atomic vapor cell. The potential wells and the band structure of the Lieb photonic lattice can be effectively manipulated by easily tuning the frequency of the involved laser beams. The current work can promisingly pave the way for exploring the exotic dynamics as well as tunable photonic devices in Lieb photonic lattices.

https://doi.org/10.1364/OL.474808

Periodic photonic structures with specific band structures have been a fertile ground to manipulate the propagation dynamics of light beams. Among the various fascinating engineered photonic band structures, flatbands, strictly dispersionless in the whole Brillouin zone [1], host significant features including complete quenching of the kinetic energy [2] and the independence of momentum. These properties have brought in remarkable beam dynamic characteristics as well as promising applications with the assistance of strongly interacting phases of matter [3,4]. By taking advantage of the flatband structures, widespread research has been inspired including slow light [5], wide-angle Klein tunneling of wave packets through potential barriers [6], Landau–Zener Bloch oscillations [7], and the realization of incompressible polaritons [8], to name a few.

As a typical photonic structure with a flatband, the Lieb lattice derived from the Hubbard model [9] builds a flatband touching two linearly dispersing bands at Dirac points, and holds a square hollow geometry with fourfold rotational symmetry [10–12]. One noteworthy feature of Lieb lattices is the quenched kinetic energy, which can suppress the transverse transport of waves due to the vanishing of the group velocity. In addition, the dispersionless energy band dominates the existence of entirely degenerate states [13]. As a consequence, high degeneracy, high density of states [12], and wave dynamics related to pseudospin [14] in Lieb photonic lattices were demonstrated. On accounts of these features, a variety of potential applications of the Lieb lattices have aroused the attention of researchers, such as suppressing the interband tunneling [15], mapping of topological singularities from momentum to real space [16], and distortion-free image transmission [17]. Up to now, a variety of optical settings (mostly based on crystalline materials) have been proved to be effective approaches [18] to realize such Lieb photonic lattices, for examples, femtosecond laser-written waveguide arrays [10,13], photorefractive crystals using a superposition of mutually incoherent square lattices [17], and frustrated lattices of micropillar optical cavities [19].

Even though flourishing achievements have been made, the current belief of the scientific community is to develop photonic structures with easily tunable bands, which support the further exploration of tunable devices for practical applications and their underlying dynamic behaviors. One commonly adopted way to improve the tunability of the currently available periodic structures is to employ the easily accessible and controllable nonlinearity in optics [20,21]. In the meanwhile, the implementation of periodic photonic structures has been expanded to alkali gaseous materials to establish instantaneously tunable electromagnetically induced photonic lattices, which have been employed to unveil novel beam dynamics [22–24] and design reconfigurable photonic devices [25,26]. Such instantaneous tunability is inherited from the real-time dynamical controllability of a laser-driven multi-level atomic medium [27].

To date, the realization of tunable electromagnetically induced photonic lattices mainly relies on optical induction methods, but is limited to several multi-beam interference patterns including regular one-dimensional lattice, hexagonal lattices, and square lattices. In principle, the Lieb photonic lattice can be implemented by combining two square lattices possessing different lattice constants with a rotation angle of 45°, but with an extraordinary cost of increasing the complexity of the practical system [10–13]. By adopting a spatial light modulator (SLM), adding binary holographic phase diagrams to generate laser beams with desired intensity profiles can break this limitation and extremely broaden the structures of electromagnetically induced photonic lattices.

In this Letter, we construct an instantaneously tunable optically induced Lieb photonic lattice with the assistance of

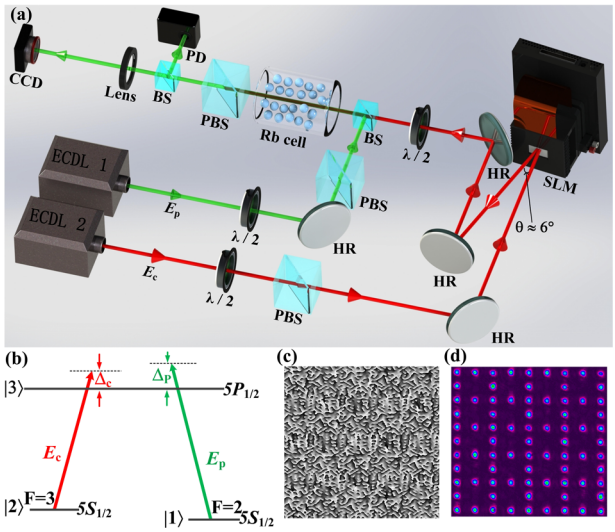

Fig. 1. (a) Experimental setup. The probe beam $\boldsymbol{E}_p$ is horizontally polarized while the coupling beam $\boldsymbol{E}_c$ is vertically polarized. A PBS cube is placed at the output plane of the vapor cell to filter the coupling beam. The probe beam is received by the CCD (via an imaging lens) and the photodiode detector (PD). The cell is filled with ^{85}Rb atomic vapor. ECDL, external cavity diode laser; SLM, spatial light modulator; $\lambda/2$, half-wave plate; PBS, polarization beam splitter; BS, beam splitter; CCD, charge coupled device camera. (b) Driven Λ-type energy-level structure; (c) Calculated holographic phase diagram loaded by the SLM for generating the Lieb coupling field. (d) Intensity distribution of the Lieb coupling field generated by the SLM.

electromagnetically induced transparency (EIT) in a coherent three-level Λ-type ^{85}Rb atomic configuration, which is excited by a strong coupling field and a co-propagating probe field. The strong coupling beam with a Lieb periodic intensity profile is generated by a phase-type SLM. When the SLM-modulated coupling field is injected to the ^{85}Rb vapor cell along the z axis, the weak Gaussian probe beam is also launched into the cell collinearly, and a 2D discrete diffraction pattern with a Lieb periodic intensity profile can be observed at the output surface in the vicinity of the EIT window. Furthermore, we explore the dynamic evolutions of the incident light under different parametric regimes. Our work broadens the way for generating more electromagnetically induced photonic lattices with desired band structures (for examples, super honeycomb and super Lieb lattices, etc.) that are not easily accessible with traditional multi-beam interference methods. Also, the realized tunable Lieb photonic lattice may provide a promising platform to explore novel bandgap properties, beam dynamics, and the design of reconfigurable photonic devices.

Figure 1(a) illustrates the experimental setup for generating an electromagnetically induced Lieb photonic lattice in the three-level ^{85}Rb atomic configuration, as depicted in Fig. 1(b). The adopted atomic configuration involving two hyperfine levels ($F = 2$ and $F = 3$, labeled as $|1\rangle$ and $|2\rangle$, respectively) is excited by the co-propagating coupling beam and probe beam from different external cavity diode lasers (ECDLs). The coupling laser beam $\boldsymbol{E}_c$ (driving the transition $|2\rangle \rightarrow |3\rangle$) from ECDL2 operating at ~795.0 nm is set as vertical polarization and injected onto the screen of the SLM, which can modulate the coupling field into a Lieb intensity profile. The horizontally polarized Gaussian probe beam $\boldsymbol{E}_p$ (connecting the transition $|1\rangle \rightarrow |3\rangle$) from ECDL1 overlaps with the coupling beam inside the Rb cell. After passing through the medium, the output probe beam is split into two components, and one is received by a charge coupled device camera to show the spatial intensity distribution while the other enters into a photodiode detector to monitor the transmitted EIT spectrum. The frequency detuning is defined as $\Delta_p = \omega_p - \omega_{31}$ and $\Delta_c = \omega_c - \omega_{32}$, where ω_i ($i = p, c$) is the frequency of laser field $\boldsymbol{E}_i$, and ω_{mn} (m, n = 1, 2, 3) is the frequency gap between states $|m\rangle$ and $|n\rangle$. The rubidium vapor cell is heated to 383 K by a covered heating tape.

During the experiment, the key point for "writing" a Lieb photonic lattice inside the sample is to modulate the spatial intensity profile of the coupling field into a Lieb geometry by the phase-only liquid crystal SLM (the resolution is 1920×1152; loaded with a 256-bit phase hologram). When aiming at generating an available phase hologram to establish a Lieb profile with multiple lattice sites, a phase only modulation may not be able to divide the intensity of the incident beam equally, referring to the traditional iterative algorithm [28]. Here, we adopt the weighted Gerchberg–Saxton algorithm, which allows to calculate nonuniform weights and average the intensity of each site via the iterative procedure. By updating the weights of each lattice site steadily, the phase hologram generated after a few tens of iterations converges to an almost uniform intensity distribution of a Lieb profile [29,30]. As a result, we obtained the holographic phase diagram given in Fig. 1(c). The laser beam with a horizontal polarization is incident into the SLM loaded with the calculated phase diagram at a small angle ($\theta \approx 6°$) to achieve the maximum efficiency for the first-level diffraction. The obtained coupling field is shown in Fig. 1(d), which exhibits a clear Lieb pattern with a high contrast between bright and dark sites.

In theory, the coupling field with a Lieb profile can engineer the desired Lieb refractive index distribution under the EIT condition. Such spatially modulated linear susceptibility can be described as

$$\chi^{(1)} = \frac{iN|\mu_{31}|^2}{\hbar\varepsilon_0} \times \frac{1}{\left(\Gamma_{31} + i\Delta_p + \frac{(\Omega_c(x,y))^2}{\Gamma_{32}+i(\Delta_p-\Delta_c)}\right)}. \quad (1)$$

In the above expression, $\Gamma_{mn} = (\Gamma_m + \Gamma_n)/2$ is the decoherence rate between states $|m\rangle$ and $|n\rangle$ with Γ_m being the transverse relaxation rate [31]; N is the atomic density at the ground state $|1\rangle$; ε_0 is the vacuum dielectric constant; $\Omega_c(x, y) = \mu_{mn}E_i/\hbar$ is the spatially distributed Rabi frequency of the coupling field generated by the SLM, in which μ_{mn} is the dipole momentum for the transition $|m\rangle$ to $|n\rangle$, and E_i is the electric-field amplitude of laser field $\boldsymbol{E}_i$.

Figures 2(a) and 2(b) demonstrate the simulated spatial refractive indices at different probe detuning Δ_p with $\Delta_c = 100$ MHz according to Eq. (1). One can see that the refractive indices show entirely inverted patterns, namely, the sites with the maximum and the minimum values (of refractive index) are exchanged when the signs of two-photon detuning $\Delta_p - \Delta_c$ are different. The propagation dynamics of the incident probe beam through the medium with a spatially engineered susceptibility is governed by the Schrödinger-like paraxial equation:

$$i\frac{\partial\psi(x,y,z)}{\partial z} = -\frac{1}{2k_0}\left(\frac{\partial^2}{\partial x^2} + \frac{\partial^2}{\partial y^2}\right)\psi - \frac{k_0}{n_0}\Delta n(x,y)\psi, \quad (2)$$

where Ψ is the envelope of the probe field $\boldsymbol{E}_p$; z is the propagation direction; $\Delta n(x, y)$ is the modulation of the refractive

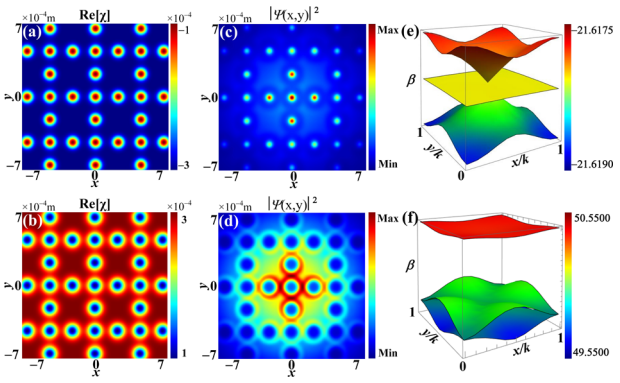

Fig. 2. Calculated refractive index patterns inside the EIT medium at (a) $\Delta_p = 110$ MHz and (b) $\Delta_p = 90$ MHz with the coupling detuning fixed at $\Delta_c = 100$ MHz. The corresponding theoretical discrete patterns of output probe fields are given in panels (c) and (d). (e) and (f) Band structures of the Lieb photonic lattices with different two-photon detunings, corresponding to panels (a) and (b). Here, β is the propagation constant; K is the width of first Brillouin zone; k_x (k_y) is the Bloch momentum normalized to K along the x (y) axis.

index imposed by the two-dimensional coupling field under EIT; $k_0 = 2\pi n_0/\lambda_p$ is the wavenumber with λ_p being the wavelength of the probe beam and $n_0 \approx 1$ being the background refractive index. This paraxial equation depicts that a weak Gaussian probe beam can be diffracted into a discrete pattern. The simulated output probe fields exiting the medium are given in Figs. 2(c) and 2(d), corresponding to the potential wells in Figs. 2(a) and 2(b), respectively. It is clear that the injected Gaussian probe field is spatially modulated into a Lieb profile for $\Delta_p - \Delta_c > 0$, while the pattern is reversed for $\Delta_p - \Delta_c < 0$.

By transforming Eq. (2) into a dimensionless equation and presuming the solution in the form $\psi(x,y,z) = u(x,y)\exp(i\beta z)$ [32], one can obtain

$$\beta u(x,y) = \frac{1}{2}\left(\frac{\partial^2}{\partial x^2} + \frac{\partial^2}{\partial y^2}\right)u(x,y) + \frac{k_0^2 r_0^2 \Delta n(x,y)}{n_0}u(x,y), \quad (3)$$

where r_0 is the typical width of the real coupling beam. By adopting numerical simulation tools, the band structures of the Lieb lattices are given in Figs. 2(e) and 2(f), with the two-photon detuning being 10 MHz and −10 MHz, respectively.

One can clearly see that the flatband emerges in the middle of the two Dirac cones in Fig. 2(e). By varying the two-photon detuning from positive $\Delta_p - \Delta_c = 10$ MHz to negative $\Delta_p - \Delta_c = -10$ MHz, the dispersionless flatband disappears and the bandgap structure is opened. Such transformation of band structures supports the easily accessible reconfigurability of the established electromagnetically induced Lieb photonic lattice.

In experiment, clear discrete patterns of the probe field can occur at the exiting plane of the cell in the range of $30\text{ MHz} \geq \Delta_p - \Delta_c \geq -20$ MHz. The detuning Δ_p of the probe field was adjusted to control the two-photon detuning as well as to realize the reconfiguration of the established Lieb photonic lattice. Such reconfigurability is manifested by the evolutions of the patterns of the output probe field passing through the induced photonic lattice. As shown in Fig. 3, the obtained probe patterns can show distinct intensity distributions by discretely varying the detuning Δ_p from 130 MHz to 80 MHz with the coupling detuning fixed at $\Delta_c = 100$ MHz. When the detuning is getting closer

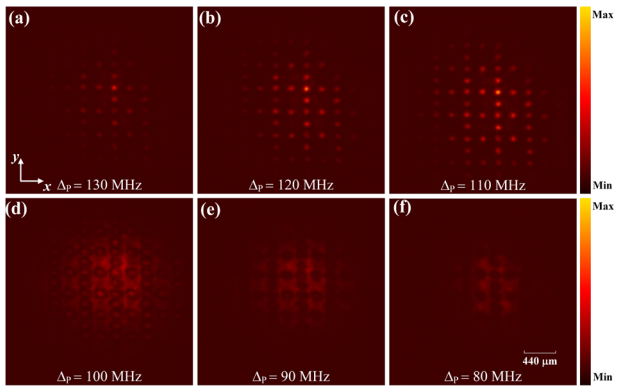

Fig. 3. Observation of discrete diffraction at different detuning of the probe field with the coupling detuning fixed at $\Delta_c = 100$ MHz. The power and size of the weak probe beam are ~1 mW and ~2 mm, respectively. The size of the Lieb coupling field is ~2.6 mm and the space between neighboring sites is ~220 μm.

to the two-photon resonance $\Delta_p - \Delta_c = 0$, the output intensity becomes stronger since EIT can suppress the resonant absorption of the probe beam most at this resonant point. It is also worth mentioning that a Gaussian profile without discrete diffraction occurs at $\Delta_p - \Delta_c = 0$ theoretically, because the modulation on the susceptibility felt by the probe field is zero, indicating the absence of spatial modulation on the refractive index. However, the observed output pattern [Fig. 3(d)] exhibits a Lieb intensity distribution superposed with an inversed-Lieb profile, which is caused by the existing linewidth (~1 MHz) of the adopted ECDL. The observation is consistent with the results without exciting the flatband eigenmode in the Lieb lattice [17,26], which supports that a Lieb-profile waveguide array has been effectively established in the sample. The evolutions of the transmitted patterns imply the modifications of the Lieb photonic lattice as well as the corresponding band structures.

Further, we experimentally reveal how the intensity of the coupling field affects the formed Lieb photonic lattice. The coupling-field intensity, determining the Rabi frequency Ω_c (x, y) in Eq. (1), can affect the modulating depth on the susceptibility. Figure 4 shows the observed diffraction patterns of the probe beam under different powers of the coupling field with the two-photon detuning being 10 MHz. With the growing of the coupling-field power, the output pattern can become clearer.

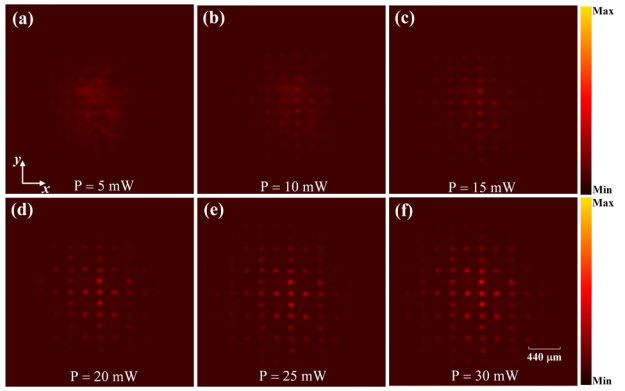

Fig. 4. Evolution of the discretized probe patterns versus the power P of the coupling field with the two-photon detuning settled as $\Delta_p - \Delta_c = 10$ MHz.

One can hardly see a Lieb profile in Fig. 4(a), because the potential well created by the weak coupling field is shallow, and the contrast between the maximum and minimum susceptibility is very small, which plays nearly the same role as a homogenous susceptibility in the atomic sample. The diffraction patterns in Figs. 4(b) to 4(f) are obtained by increasing the coupling power from 10 mW to 30 mW with the two-photon detuning being $\Delta_p - \Delta_c = 10$ MHz. For a weak coupling laser with P being less than 15 mW, fuzzy discretized patterns occur in Figs. 4(b) and 4(c). The fuzzy patterns with a very low contrast between the bright and dark sites arise from the relatively small modulation on the susceptibility, and the coupling strength between lattice channels is not strong enough to "attract" the whole probe energy into an individual waveguide to form a clearly discrete pattern. The contrast and intensity of diffraction patterns are gradually improved with the power increasing above 20 mW, as shown in Figs. 4(d)–4(f). In Fig. 4(f) with P = 30 mW, the discretized pattern shows no obvious change compared to that in Fig. 4(e), and the reason is twofold: the first one is that the coupling between the lattice channels is strong enough to make the probe beam completely travel inside the waveguides for P = 25 mW; the second one is probably due to the depletion of particles in the ground state $|1\rangle$, and the efficiency of the EIT can experience little enhancement for higher coupling powers.

In conclusion, by introducing an SLM to realize a desired coupling intensity profile, we have established an instantaneously reconfigurable Lieb photonic lattice in a coherently prepared three-level atomic medium. Such an electromagnetically induced Lieb photonic lattice is not easily generated by the conventional multi-beam interference method. We also demonstrate the evolution of the potential wells of the induced Lieb photonic lattice by easily adjusting the laser parameters. The evolution is reflected by the change of the output discrete patterns of the incident probe field traveling though the medium, indicating the readily accessible reconfigurability of the formed photonic structure. The current work provides an alternative way to engineer tunable Lieb photonic lattices, which may become a promising platform for investigating the underlying beam dynamics and tunable photonic devices relying on flatband structures.

Disclosures. The authors declare no conflicts of interest.

Data availability. Data underlying the results presented in this paper are not publicly available at this time but may be obtained from the authors upon reasonable request.

REFERENCES

1. S. Xia, A. Ramachandran, S. Xia, D. Li, X. Liu, L. Tang, Y. Hu, D. Song, J. Xu, D. Leykam, S. Flach, and Z. Chen, Phys. Rev. Lett. **121**, 263902 (2018).
2. Y. He, R. Mao, H. Cai, J. Zhang, Y. Li, L. Yuan, S. Zhu, and D. Wang, Phys. Rev. Lett. **126**, 103601 (2021).
3. D. Călugăru, A. Chew, L. Elcoro, Y. Xu, N. Regnault, Z. Song, and B. A. Bernevig, Nat. Phys. **18**, 185 (2022).
4. D. Leykam, A. Alexei, and F. Sergej, Adv. Phys.: X **3**, 1473052 (2018).
5. T. Baba, Nat. Photonics **2**, 465 (2008).
6. R. Shen, L. Shao, B. Wang, and D. Xing, Phys. Rev. B **81**, 041410 (2010).
7. R. Khomeriki and S. Flach, Phys. Rev. Lett. **116**, 245301 (2016).
8. M. Biondi, E. P. L. van Nieuwenburg, G. Blatter, S. D. Huber, and S. Schmidt, Phys. Rev. Lett. **115**, 143601 (2015).
9. E. H. Lieb, Phys. Rev. Lett. **62**, 1201 (1989).
10. S. Mukherjee, A. Spracklen, D. Choudhury, N. Goldman, P. Öhberg, E. Andersson, and R. R. Thomson, Phys. Rev. Lett. **114**, 245504 (2015).
11. Y. Chang, Y. Lu, Y. Wang, X. Xu, W. Zhou, W. Cui, X. Wang, J. Gao, L. Qiao, and X. Jin, Phys. Rev. Lett. **126**, 110501 (2021).
12. D. Guzmán-Silva, C. Mejía-Cortés, M. A. Bandres, M. C. Rechtsman, S. Weimann, S. Nolte, M. Segev, A. Szameit, and R. A. Vicencio, New. J. Phys. **16**, 063061 (2014).
13. R. A. Vicencio, C. Cantillano, L. Morales-Inostroza, B. Real, C. Mejía-Cortés, S. Weimann, A. Szameit, and M. I. Molina, Phys. Rev. Lett. **114**, 245503 (2015).
14. F. Diebel, D. Leykam, S. Kroesen, C. Denz, and A. S. Desyatnikov, Phys. Rev. Lett. **116**, 183902 (2016).
15. V. Apaja, M. Hyrkäs, and M. Manninen, Phys. Rev. A **82**, 041402 (2010).
16. X. Liu, S. Xia, E. Jajtić, D. Song, D. Li, L. Tang, D. Leykam, J. Xu, H. Buljan, and Z. Chen, Nat. Commun. **11**, 1586 (2020).
17. S. Xia, Y. Hu, D. Song, Y. Zong, L. Tang, and Z. Chen, Opt. Lett. **41**, 1435 (2016).
18. L. Tang, D. Song, S. Xia, S. Xia, J. Ma, W. Yan, Y. Hu, J. Xu, D. Leykam, and Z. Chen, Nanophotonics **9**, 1161 (2020).
19. F. Baboux, L. Ge, T. Jacqmin, M. Biondi, E. Galopin, A. Lemaître, L. Le Gratiet, I. Sagnes, S. Schmidt, H E Türeci, A. Amo, and J. Bloch, Phys. Rev. Lett. **116**, 066402 (2016).
20. D. A. Dobrykh, A. V. Yulin, A P Slobozhanyuk, A. N. Poddubny, and Y. S. Kivshar, Phys. Rev. Lett. **121**, 163901 (2018).
21. Y. V. Kartashov and D. V. Skryabin, Phys. Rev. Lett. **122**, 083902 (2019).
22. Z. Zhang, S. Liang, F. Li, S. Ning, Y. Li, M. Guillaume, Y. Zhang, M. Xiao, and D. Solnyshkov, Optica **7**, 455 (2020).
23. Z. Zhang, F. Li, G. Malpuech, Y. Zhang, O. Bleu, S. Koniakhin, C. Li, Y. Zhang, M. Xiao, and D. Solnyshkov, Phys. Rev. Lett. **122**, 233905 (2019).
24. Z. Zhang, R. Wang, Y. Zhang, Y. V. Kartashov, F. Li, H. Zhong, H. Guan, K. Gao, F. Li, Y. Zhang, and M. Xiao, Nat. Commun. **11**, 1902 (2020).
25. J. Yuan, S. Dong, C. Wu, L. Wang, L. Xiao, and S. Jia, Opt. Express **28**, 23820 (2020).
26. J. Sheng, J. Wang, M. A. Miri, D. N. Christodoulides, and M. Xiao, Opt. Express **23**, 19777 (2015).
27. S. Taie, H. Ozawa, T. Ichinose, T. Nishio, S. Nakajima, and Y. Takahashi, Sci. Adv. **1**, e1500854 (2015).
28. R. W. Gerchberg and W. O. Saxton, Optik **35**, 275 (1971).
29. R. D. Leonardo, F. Ianni, and G. Ruocco, Opt. Express **15**, 1913 (2007).
30. S. Bianchi and R. D. Leonardo, Comput. Phys. Commun. **181**, 1444 (2010).
31. Z. Zhang, X. Liu, D. Zhang, J. Sheng, Y. Zhang, Y. Zhang, and M. Xiao, Phys. Rev. A **97**, 013603 (2018).
32. Y. Kang, H. Zhong, M. R. Belić, Y. Tian, K. Jin, Y. Zhang, F. Li, and Y. Zhang, Ann. Phys. **531**, 1900295 (2019).